JOURNAL OF SOLID STATE CHEMISTRY 118, 133–140 (1995)

Structures in the Oxygen-Deficient Fluorite-Related R_nO_{2n-2} Homologous Series: Pr_9O_{16}

J. Zhang, R. B. Von Dreele,* and L. Eyring

*Department of Chemistry and Biochemistry and the Center for Solid State Science, Arizona State University, Tempe, Arizona 85287-1604; and *Manuel Lujan, Jr. Neutron Scattering Center, LANSCE, MS H805, Los Alamos National Laboratory, Los Alamos, New Mexico 87545*

Received April 8, 1994; in revised form January 13, 1995; accepted January 19, 1995

The crystal structure of the lower-temperature polymorph of the $n = 9$ member of the homologous series Pr_nO_{2n-2}, Pr_9O_{16} (ζ), was determined utilizing Rietveld analysis of neutron time-of-flight powder diffraction data. The refined structure ($P\bar{1}$, $a = 6.7396(8)$ Å, $b = 8.711(1)$ Å, $c = 6.6726(8)$ Å, $\alpha = 97.424(1)°$, $\beta = 99.973(1)°$, $\gamma = 75.301(1)°$, $V = 371.7(1)$ Å^3; $Z = 1$; $R_p = 3.29\%$, and $wR_p = 4.64\%$) is in agreement with the model proposed on the basis of high-resolution electron microscopy. This structure is a superstructure of fluorite (F). The structural element is a pair of vacant oxygen sites separated by $\frac{1}{2}[111]_F$ across a metal atom. These units are further apart from each other than those in the more reduced member of the series, Pr_7O_{12}. The existence of a higher-temperature form of Pr_9O_{16} was not confirmed. © 1995 Academic Press, Inc.

INTRODUCTION

The higher oxides of the rare earth elements (RO_x, R = Ce, Pr, Tb, $1.5 < x < 2.0$) are electron and fast oxygen ion conductors and are potential oxygen sensors (1). They are closely related to other important ceramic materials whose structures are derived from fluorite (e.g., stabilized zirconia). Detailed studies of these rare earth oxides may be dated back to the 1950's (2–5). Thermodynamic studies reveal rich structure-related phenomena, including the formation of ordered intermediate phases at low temperatures and grossly nonstoichiometric disordered compounds at higher temperatures and pressures (1–6). These systems form structurally related phases whose transitions offer unique opportunities to study composition, defect structure, and property relationships.

There have been persistent efforts to elucidate the structures of the ordered phases in such a way that the underlying principles of oxygen defect formation, ordering, and phase transitions in these fluorite-related compounds might be understood. It has not been possible to grow single crystals suitable for structure determination utilizing X-rays in these heavy-metal oxides. Analysis of X-ray powder diffraction patterns has provided phase identification (6, 7). The superstructure lines are sometimes too weak to be observed, hence, the positions and splitting of the substructure fluorite lines are used to identify the phase. Electron microscopy has become a powerful method in identifying new phases and deriving unit cells (8). However, information beyond the unit cell level has been proven less reliable for these rare earth oxides, due to problems such as resolution limits, possible beam tilt, dynamic scattering, and radiation damage. In the meantime, investigations involving topological analysis (9–12) or group theory (13) were also conducted, yet the accuracy of the predicted models was poor because of the lack of adequate data and the large number of possibilities.

Neutron powder diffraction, in combination with Rietveld analysis, has become a powerful technique in clarifying such difficult structural problems. The large neutron scattering length for oxygen makes it possible to locate vacancies in the oxygen sublattice. Structural characterization of Pr_7O_{12} (14) was a successful example of these techniques. However, studies on the CeO_x systems (15) suggested that improved resolution and adequate modeling were essential when larger and more complex structures were under consideration. Recently, high-resolution neutron time-of-flight (TOF) powder diffraction and improved software, GSAS, based on Rietveld analysis, have become available (16). Taking advantage of this, Tb_7O_{12} and $Tb_{11}O_{20}$ have recently been structurally characterized (17).

Among the rare earth higher oxides, the Pr_nO_{2n-2} (n = 7, 9, 10, 11, 12) homologous series has the largest number of known intermediate phases and many of them do not require extreme preparation conditions. Pr_9O_{16} (ζ) was selected for this study. Previous X-ray powder diffraction studies indicated that there might be two forms of Pr_9O_{16}, based on the splitting patterns of the $\{111\}_F$ reflection (6). It was suggested that quenched samples might be rhombohedral, while samples annealed at lower temperatures were triclinic. In addition, a TGA decomposition record also indicated a change of slope that could be interpreted as a phase transition between the two forms.

0022-4596/95 $12.00

The unit cell of the triclinic Pr_9O_{16} was established by electron microscopy (8). This lower-temperature form of Pr_9O_{16} has two axes, a and c, in common with Pr_7O_{12} (ι), Tb_7O_{12} (ι) and $Tb_{11}O_{20}$ (δ), and contains one atomic formula per unit cell. A model was proposed for the triclinic Pr_9O_{16} by Tuenge and Eyring (18) based on electron microscopy and image simulation.

EXPERIMENTAL

Sample preparation. The starting material, Pr_6O_{11} (Research Chemicals Inc., 5N), was heated at 1000°C for several hours to remove possible carbonate and hydroxide contamination formed during storage. The resulting sample was light green, characteristic of A-type Pr_2O_3. On the basis of previous thermodynamic studies, the composition was adjusted to Pr_9O_{16} by annealing the sample under 10 Torr of O_2 at 560°C for 5 days to ensure homogeneity. In order to avoid mixing of different polymorphs, a sample was sealed off at room temperature *in vacuo*, and further annealed at 400°C for 60 days to form the lower-temperature Pr_9O_{16}. Two other samples were annealed at higher temperatures (575°C, P_{O_2} (25°C) = 7 Torr, 60 days, slow cooled; 560°C, P_{O_2} (560°C) = 10 Torr, 5 days, quenched in water) in an effort to prepare and capture the higher-temperature form of Pr_9O_{16}.

The samples thus prepared were kept under an inert atmosphere and transferred to airtight vanadium cans for neutron diffraction studies.

Neutron diffraction and Rietveld analysis. The neutron TOF diffraction data were collected at room temperature on the high-resolution instrument (NPD) at the Manuel Lujan, Jr. Neutron Scattering Center at Los Alamos National Laboratory. Each data set comprises four spectra from detectors at 2θ of $\pm 148°$ and $\pm 90°$, respectively. The Rietveld refinements were performed utilizing the GSAS structure analysis package (16).

The structure determination of the low-temperature Pr_9O_{16} employed the structure proposed by Tuenge and Eyring (18) as the initial model. After the spectrum coefficients, such as background, scale factors, diffractometer constants, and profile coefficients, were refined, the structural parameters were varied. The lattice constants were essentially identical to those expected. To reduce the number of variables, the thermal factors of like atoms were refined as one parameter. The atoms experienced minor shifts when the positional parameters were refined, and the resulting interatomic distances were reasonable. The calculated spectra are in good agreement with those observed (see Fig. 1), and the low values of R_p, wR_p, and reduced χ^2 also confirmed the reliability of the refinement.

Careful examination of the difference curves suggested the presence of a second phase with a smaller fluorite subcell, and the extra superstructure peaks corresponded to those of $Pr_{10}O_{18}$. Further refinement confirmed that there was about 10 mol% of $Pr_{10}O_{18}$ in the sample. Although introducing this second phase improved the refinement statistics, it had very little effect on the structure of Pr_9O_{16}. Therefore, the single phase model was adopted for the final stage of the refinement, because involving $Pr_{10}O_{18}$ introduced too many additional variables.

Refinements on data from two samples annealed at higher temperatures showed that both contained the low-temperature Pr_9O_{16} and $Pr_{10}O_{18}$ in about equal proportions. In addition, a minor phase(s) of about 10 at.% might also be present, since the refinements with the two-phase models did not reach satisfactory levels. The identification of this third phase was difficult due to its small percentage, and the fact that the data-to-variables ratio had become too low.

RESULTS AND DISCUSSION

The structure of the low-temperature form of Pr_9O_{16}. The refinement parameters for the lower-temperature form of Pr_9O_{16} are given in Table 1. The refined atomic parameters and important interatomic distances in Pr_9O_{16} are reported in Tables 2 and 3, respectively.

TABLE 1
Important Refinement Parameters for Pr_9O_{16}

Diffractometer	NPD		
No. of data in four spectra	26002		
Min. d-spacing (Å)	0.5		
Model	100% Pr_9O_{16}		
Space group	$P\bar{1}$		
Lattice constants:			
a, b, c (Å)	6.7396(8)	8.711(1)	6.6726(8)
α, β, γ (°)	97.424(1)	99.973(1)	75.301(1)
V (Å^3)	371.7(1)		
Z	1		
Variables			
Structural:			
Lattice	6		
Positional	36		
Thermal	2 (Linked)		
Other			
Absorption	1		
Background	36		
Diffractometer	11		
Profile (Gaussian)	8		
Scale	4		
Total	104		
wR_p (%)[a]	4.64		
R_p (%)[a]	3.29		
χ^2 (reduced)[a]	1.154		

[a] $wR_p = [w\Sigma(I_o-I_c)^2/\Sigma wI_o^2]^{1/2}$.
$R_p = \Sigma|I_o-I_c|/\Sigma I_o$.
$\chi^2 = \Sigma w(I_o-I_c)^2/(N_{obs}-N_{var})$.

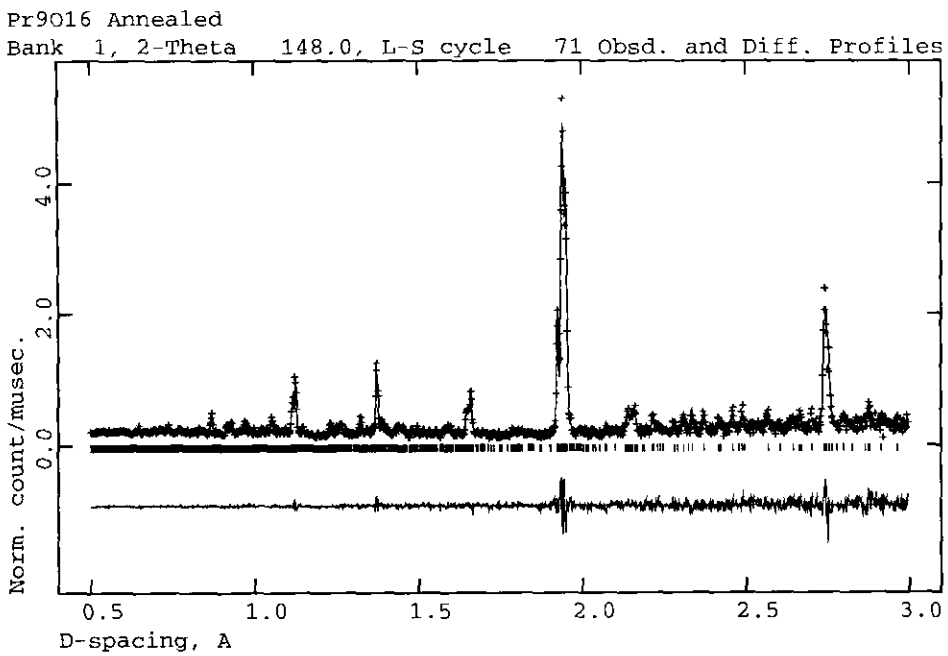

FIG. 1. The observed (crosses) and calculated (solid line) powder neutron diffraction profiles for Pr_9O_{16} (ζ), normalized by the incident intensity spectrum. The Bragg positions are marked.

Figure 2a illustrates the relationship between the fluorite substructure and that of the ideal zeta phase. Figure 2b shows the [100] projection of the real structure.

Pr_9O_{16} (ζ) and Pr_7O_{12} (ι) share two common axes, a and c, and each has two vacant oxygen sites, $\square_O$, per unit cell. The relationships of these two phases to the parent fluorite structure are represented by:

$$a_\iota = \tfrac{1}{2}(2a_F + b_F - c_F) \qquad a_\zeta = \tfrac{1}{2}(2a_F + b_F - c_F)$$
$$b_\iota = \tfrac{1}{2}(-a_F + 2b_F + c_F) \qquad b_\zeta = \tfrac{1}{2}(\quad + 3b_F + c_F)$$
$$c_\iota = \tfrac{1}{2}(\ a_F - b_F + 2c_F) \qquad c_\zeta = \tfrac{1}{2}(\ a_F - b_F + 2c_F)$$

TABLE 2
Positional and Thermal Parameters for Pr_9O_{16}

Atom	x	y	z	$U_{iso} \times 100$ (Å^2)[a] (Linked)
Pr(1)	0	0	0	0.49(1)
Pr(2)	0.2326(4)	0.1006(3)	0.5871(3)	0.49(1)
Pr(3)	0.4740(4)	0.2281(2)	0.1121(4)	0.49(1)
Pr(4)	0.8754(3)	0.4698(3)	0.2312(4)	0.49(1)
Pr(5)	0.6796(4)	0.3321(3)	0.6631(4)	0.49(1)
O(1)	0.8089(3)	0.2555(2)	0.0348(3)	0.93(1)
O(2)	0.1834(3)	0.4418(2)	0.1300(3)	0.93(1)
O(3)	0.2938(3)	0.0408(2)	0.9414(3)	0.93(1)
O(4)	0.5924(3)	0.4251(2)	0.3271(3)	0.93(1)
O(5)	0.4977(3)	0.1457(2)	0.4048(3)	0.93(1)
O(6)	0.0016(3)	0.3464(2)	0.5344(3)	0.93(1)
O(7)	0.9099(3)	0.0589(2)	0.6787(3)	0.93(1)
O(8)	0.3904(3)	0.2947(2)	0.8015(3)	0.93(1)
$\square_O$	5/36	7/36	2/9	—

[a] The form of the isotropic displacement parameter is $T = \exp[-8\pi^2 U_{iso} \sin^2\theta/\lambda^2]$.

In Pr_7O_{12}, the beginning member of the Pr_nO_{2n-2} series, the shortest separation of oxygen vacant sites is $\frac{1}{2}[111]_F$. The vacancy pairs, separated by $\frac{1}{2}[111]_F$, may be divided into two types (Fig. 3a): type A, with a metal cation between the vacancies, and type B, without. In the more oxidized intermediate phase Pr_9O_{16}, certain $\square_O$–$\square_O$ distances become larger, corresponding to a longer b axis. By keeping the a and c axes identical to those of Pr_7O_{12}, two models for Pr_9O_{16} may be derived from Pr_7O_{12}. The first (Fig. 3b) is obtained by preserving the fragment of the A-type, while increasing the distances between vacancies of the B-type to $\frac{1}{2}[012]_F$. The second model (Fig. 3c) corresponds to eliminating pairs of type A by moving them away from each other while preserving the B-type sites. In addition to these two models, there is a third possible structure for Pr_9O_{16} under the constraints of the unit cell dimensions and the $P\bar{1}$ symmetry, as was discussed by Tuenge and Eyring (18). Although its unit cell is the same as the other two models, its orientation is different. Its relationship to Pr_7O_{12} and the fluorite subcell may be represented as (Fig. 3d):

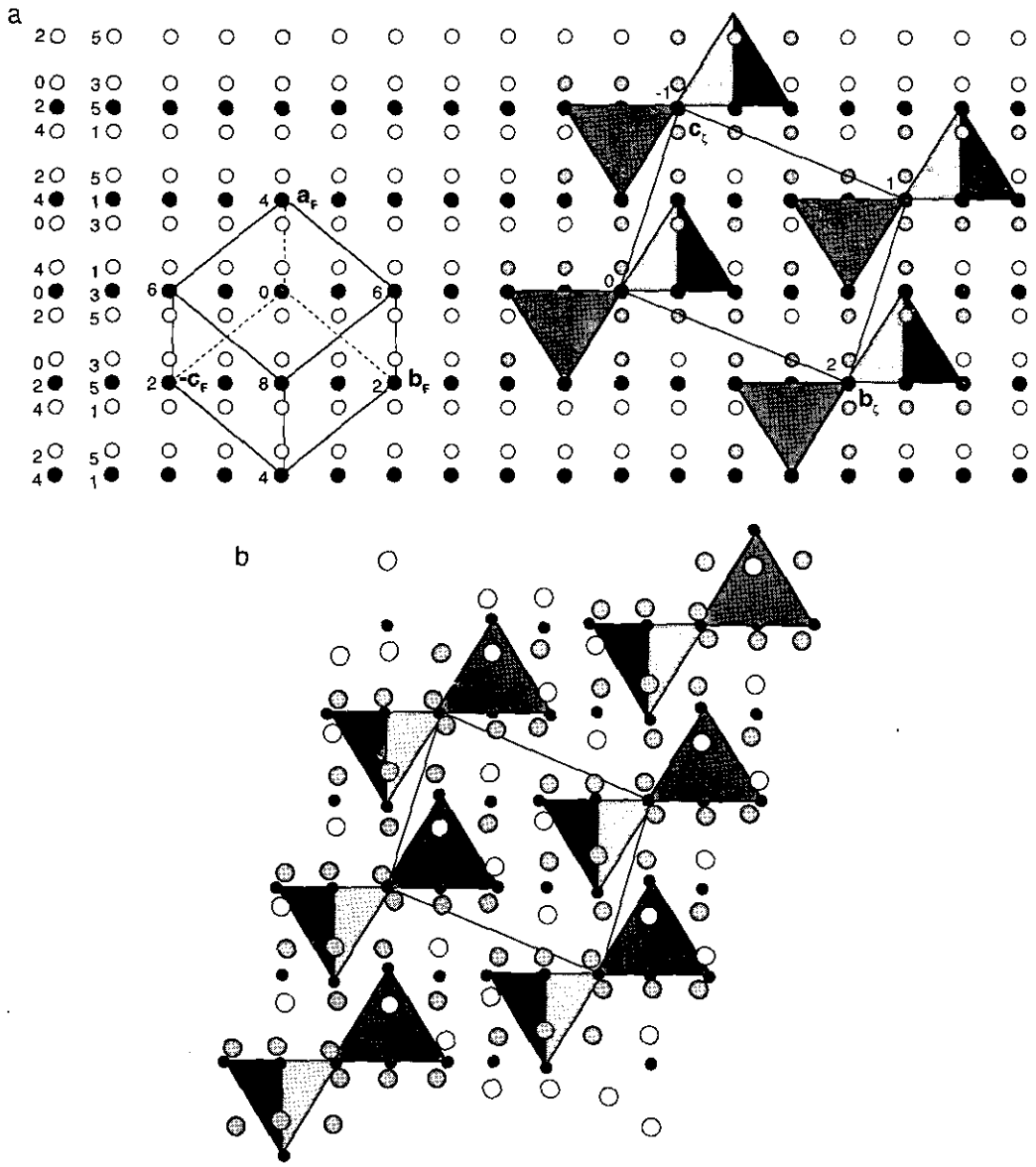

FIG. 2. (a) The net of spots on the left represents the fluorite structure in the [2 1 $\bar{1}$] projection. The metal atom representations are shaded. The fluorite unit cell is sketched. The numbers by the corner metal atoms indicate their relative heights in units of sixths of $\frac{1}{6}$[2 1 $\bar{1}$]. The fluorite axes coincide with the dashed lines. The model on the right maps the tetrahedrally coordinated vacant oxygen sites in an ideal lattice of the Pr_9O_{16} structure suggesting the supercell. (b) The $[100]^{\zeta} = \frac{1}{2}[2\ 1\ \bar{1}]_F$ ORTEP projection of the real structure of Pr_9O_{16}. The large circles represent oxygen atoms and the smaller ones represent praseodymium atoms. The Pr_4 groups around the oxygen vacancies ($\square_O$) are outlined.

$$
\begin{aligned}
a_\zeta &= a_\iota &&= \tfrac{1}{2}(2a_F + b_F - c_F)\\
b_\zeta &= b_\iota + c_\iota &&= \tfrac{1}{2}(\quad + b_F + 3c_F)\\
c_\zeta &= c_\iota + \tfrac{1}{2}[0\bar{1}\bar{1}]_F &&= \tfrac{1}{2}(a_F - 2b_F + c_F).
\end{aligned}
$$

This structure contains the same $[111]_F$ strings of vacancy pairs as those in Pr_7O_{12}, but with a greater separation between the strings. The fact that the observed structure of the low-temperature Pr_9O_{16} corresponds to the first model suggests that this structure with vacancy pairs across a metal atom is the most stable one at relatively low temperatures. Furthermore, of the two models (Figs. 3b and 3d) having double-vacancy defects of type A, the one with the strings along $[111]_F$ (Fig. 3d) is evidently less stable since it also has a B-type vacancy arrangement.

By comparing the average Pr–O distances (Table 3) with the corresponding summation of crystal radii (19), a relative charge distribution in the cation lattice of Pr_9O_{16} may be assigned. Cations that are neighbors of anion vacancies have higher formal charges than those further away. This conclusion is based upon the relationship

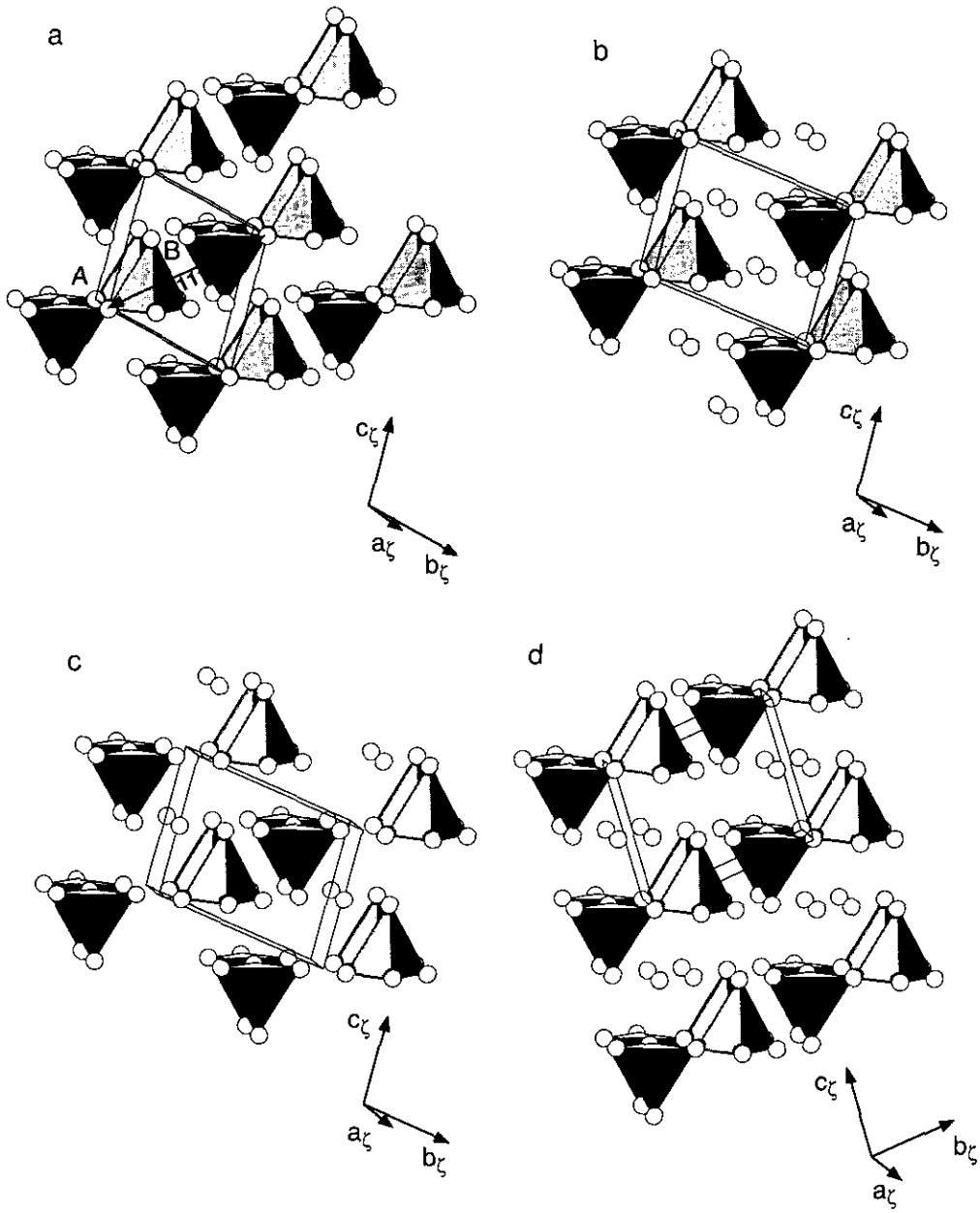

FIG. 3. The near $[2\,1\,\bar{1}]_F$ *view of (a)* Pr_7O_{12}; *(b)* Pr_9O_{16} *model I; (c)* Pr_9O_{16} *model II; (d)* Pr_9O_{16} *model III. The oxygen atoms are omitted for clarity, and the* Pr_4 *tetrahedra around oxygen vacancies are emphasized.*

between the coordination numbers (CN) and the cation sizes. For example, the average Pr(1)–O distance is in good agreement with the value expected for a Pr^{4+} cation with a CN of 6 as indicated in footnote "*a*" of Table 3. This same feature is observed for Pr_7O_{12} and other fluorite-related mixed-valent oxides. The 6-coordinated cation, situated between a pair of oxygen vacancies, is the smallest in a given structure. Thornber and Bevan (20) have concluded that among fluorite-related ternary (pseudobinary) oxides, such as UY_6O_{12}, ULu_6O_{12}, and low-temperature $Zr_3Yb_4O_{12}$, where the metal atoms are ordered, the more highly charged cation occupies the position of lowest coordination. Furthermore, they find that cation size is more important than charge in the determination of the occupancy of these sites since in $Zr_3Sc_4O_{12}$, where the cation sizes are the same, there is no occupancy preference. Pr(5), which is a part of the PrO_2 fragment separating vacancy clusters, has a CN of 8 and the longest Pr–O distances, hence, must have the lowest charge (Pr^{+3}) (Table 3).

Although less significant, there is a compensating effect that minimizes the charge segregation and the strain introduced by distortions from the parent fluorite structure. Among the cations that have the same number of oxygen and vacancy neighbors, those nearest the Pr^{4+}'s bear lower formal charges. This could account for the charge differences among the other three independent cations that are 7-coordinated. They all have average Pr–O distances between those expected for Pr^{4+} and Pr^{3+}; therefore, they should carry intermediate valences consistent with the bond distances and the required charge balance of the system. In Pr_7O_{12}, the 7-coordinated cations are related by symmetry, but in Pr_9O_{16} they could bear different charges. Pr(2) has the most Pr^{4+} neighbors and the longest Pr–O distances and therefore a lower charge. In contrast, Pr(3) and Pr(4) have more Pr^{3+} neighbors and higher formal charges. The collective effect of these two contradicting factors is a net charge separation with the defect-cores bearing positive charges. This picture differs from a previous one (12) which had the two electrons generated by the loss of oxygen,

$$O^{2-} \rightarrow \tfrac{1}{2}O_2 + 2e^-,$$

reduce the nearest cations, and therefore a vacant oxygen site would carry little or no charge.

The charge assignment above suggests the three 7-coordinated Pr cations carry intermediate valences. Yet, a recent X-ray absorption spectroscopic study by Karnatak (21) concluded that there are no intermediate valences in the rare earth higher oxides, i.e. the cations change their valences abruptly with their CN. It is important, however, to realize that these apparently contradictory results are obtained from quite different experimental situations. On one hand, the X-ray absorption study registered the electron transfer between different states. Because these states are associated with electrons in the contracted *f*-orbitals, the influence of the crystal field has little effect. At any given instant, the excited electron is localized on one particular nucleus, giving signals corresponding to either a +3 or +4 state. On the other hand, the neutron diffraction data for Pr_9O_{16} were collected over about 1 day. The structure elucidated using this information must reflect an average structure. The fact that the 7-coordinated cations carry formal intermediate charges may be understood to be the consequence of fast electron hopping reflected in the observed electronic semiconduction (22). It would also contribute to the entropy increase of the system.

Keep in mind that although the defect-free region has the composition and metal-atom coordination of PrO_2, the bond distances suggest that the Pr cation is +3 instead of +4; hence the region bears a local negative charge. If the observed $\square_O$–O and $\square_O$–Pr distances are compared with the average O–O and O–Pr distances in Pr_9O_{16}, one can also conclude that the oxygen vacancies are positively charged. In the fluorite structure, each anion may be viewed as occupying an octahedral site formed by its six nearest anion neighbors. At the same time, the anion sits at the center of a tetrahedron formed by its four neighboring cations. In Pr_9O_{16}, the distances between a

TABLE 3
Important Interatomic Distances in Pr_9O_{16}

Atom 1	Atom 2	Mult.	Distance (Å)	Atom 1	Atom 2	Mult.	Distance (Å)
			Pr coordination environment				
Pr(1)	O(1)	2	2.282(2)	Pr(2)	O(3)	1	2.438(3)
CN 6	O(3)	2	2.195(2)	CN 7	O(5)	1	2.432(4)
[+4][a]	O(7)	2	2.211(3)		O(5)	1	2.462(3)
	Average		2.229		O(6)	1	2.338(4)
					O(7)	1	2.483(3)
Pr(3)	O(1)	1	2.471(4)		O(7)	1	2.345(4)
CN 7	O(2)	1	2.335(4)		O(8)	1	2.396(3)
	O(3)	1	2.489(4)		Average	1	2.413
	O(3)	1	2.349(4)				
	O(4)	1	2.312(4)	Pr(4)	O(1)	1	2.228(4)
	O(5)	1	2.148(4)	CN 7	O(2)	1	2.554(3)
	O(8)	1	2.168(4)		O(2)	1	2.258(3)
	Average		2.325		O(4)	1	2.252(4)
					O(6)	1	2.297(4)
Pr(5)	O(1)	1	2.604(4)		O(7)	1	2.346(3)
CN 8	O(2)	1	2.540(4)		O(8)	1	2.357(4)
[+3][a]	O(4)	1	2.417(4)		Average		2.327
	O(4)	1	2.389(4)				
	O(5)	1	2.568(4)				
	O(6)	1	2.515(4)				
	O(7)	1	2.500(4)				
	O(8)	1	2.403(4)				
	Average		2.492				
			O vacancy cluster				
$\square_O$	Pr(1)	1	2.372(1)	Pr(1)	Pr(2)	1	4.034(3)
	Pr(2)	1	2.591(2)		Pr(3)	1	4.098(3)
	Pr(3)	1	2.599(3)		Pr(4)	1	4.113(3)
	Pr(4)	1	2.602(3)	Pr(2)	Pr(3)	1	4.200(4)
	Average		2.541		Pr(4)	1	4.231(4)
				Pr(3)	Pr(4)	1	4.221(4)
$\square_O$	O(1)	1	2.326(3)		Average[b]		4.150
	O(2)	1	2.422(2)				
	O(3)	1	2.384(3)				
	O(5)	1	2.477(3)				
	O(6)	1	2.510(2)				
	O(7)	1	2.502(2)				
	Average		2.437				

[a] The charges are assigned by comparing the average distances with the corresponding summation of crystal radii (19):

Pr^{+m}	CN = 6	CN = 7	CN = 8
m = +3	2.37 (Å)	2.44 (Å)	2.506 (Å)
m = +4	2.23 (Å)	2.29 (Å)	2.34 (Å)

[b] The value is the average within the $\square_O P_4$ group.

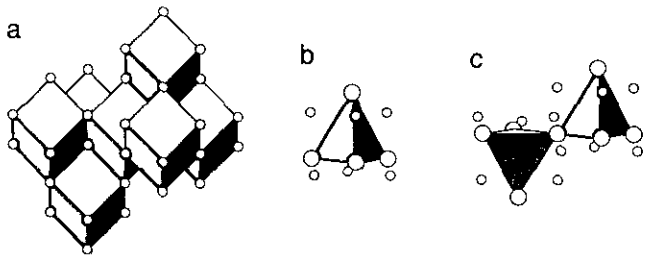

FIG. 4. The near $[2\ 1\ \bar{1}]_F$ representations of (a) Bevan cluster, $(\square_O)_2Pr_7O_{36}$, with the PrO_8 cubes shown; (b) the coordination defect, $\square_OPr_4O_6$, with the $\square_OPr_4$ tetrahedron shown; (c) two coordination defects sharing a Pr, $(\square_OPr_{3+1/2}O_6)_2$.

vacancy and its nearest oxygen neighbors are about 0.3 Å shorter than the average O–O distances in fluorite dioxide, while Pr cations, except for the one between the pair of vacancies, are moved away from the vacancy by about 0.2 Å,. These distortions are consistent with positively charged vacant oxygen sites. A similar phenomenon was observed for Pr_7O_{12}, although the magnitude was smaller.

Because defect formation involves not just one isolated oxygen site, but also the surrounding lattice, the structures can be described in terms of defect clusters. Three cluster models have previously been proposed for these fluorite-related rare earth oxide systems. One is the popular double-vacancy cluster, frequently referred to as the Bevan cluster (23, 24). This model suggests that the vacant oxygen sites occur in pairs, and each cluster involves 7 cations and 36 anions, $(\square_O)_2Pr_7O_{36}$ (Fig. 4a). In Pr_7O_{12}, such clusters are closely packed, and every cation in the structure is part of a vacancy cluster. In Pr_9O_{16}, on the other hand, the clusters are separated by $Pr^{3+}O_2$ fragments that are not parts of clusters. Although all of the known fluorite-related ceramic systems, such as stabilized zirconia, also have these double vacancies as basic structural elements (24, 25), their importance in modeling the structures of the rare earth oxides may have been overemphasized. A second, simpler basic defect cluster, introduced by Martin (9), is a coordination defect consisting of one vacant oxygen site, 6 surrounding oxygens in sites moved closer to the vacancy, and 4 cations in sites moved away from the vacancy (Fig. 4b). Overlapping of the oxygen atom positions from different clusters is not favorable in energy for low concentrations of these defect clusters. The third type has a tetrahedral defect core that consists of a vacancy and its 4 cation neighbors. It has been suggested that the intermediate phases are built up of clusters with the same core but of various sizes, and the size of the clusters decreases with an increase in cluster concentration (12). Since a larger defect cluster may be viewed as a smaller one plus its surroundings with the fluorite composition, the isolated coordination defect defined by Martin (9) is more convenient to consider in practice.

The Bevan cluster itself may also be viewed as two simple coordination defects sharing one common cation, $(\square_OPr_{(3+1/2)}O_6)_2$ (Fig. 4c). Although either the double vacancy model or the coordination defect model (except that these may not share oxygens) may be employed to rationalize the structures of Pr_7O_{12}, Tb_7O_{12}, and Pr_9O_{16}, as oxidation progresses, the double vacancy clusters dissociate into single vacancy clusters. For example, in $Tb_{11}O_{20}$ (17) and $Pr_{12}O_{22}$ (26, 27), the structures can only be described utilizing the coordination defect.

Another way of representing the structures of Pr_7O_{12} and Pr_9O_{16} is in terms of the stacking of cluster layers. As a result of sharing common *a* and *c* axes, layers in the (010) directions for both structures coincide with the $(1\ \bar{5}\ \bar{3})_F$ planes. These layers may be viewed as slabs consisting of double vacancies or combined single coordination defects. In Pr_7O_{12}, the slabs are stacked upon one another, whereas in Pr_9O_{16}, they are separated by the insertion of layers with PrO_2 composition. If this modeling is extended to include the structure of $Tb_{11}O_{20}$ (16), the common structural elements are (010) slabs consisting of single layers of coordination defects.

The experiments on the high-temperature form of Pr_9O_{16}. Although no conclusive results could be drawn from the studies on samples annealed at higher temperatures, the heat treatment did have a significant effect on the material. Regardless of the cooling rates, annealed samples contained the low-temperature form of Pr_9O_{16} and $Pr_{10}O_{18}$, plus an unidentified phase in lower relative amounts. One explanation is that a high-temperature modification was formed at the annealing temperatures, but was partially or completely converted to other phases during cooling. This is conceivable since the transition of intermediate phases in these systems only involves rearrangement of the oxygen vacancies, which is a very fast process at elevated temperatures. Since the low-temperature sample, annealed at 400°C, also had about 10 mol% of $Pr_{10}O_{18}$, one must assume that the original preparation had picked up oxygen during cooling before the various samples were sealed off for annealing, thus shifting the stoichiometry.

Since quenching the high-temperature form of Pr_9O_{16} for neutron diffraction study was not successful, it seems necessary to conduct high-temperature, *in situ* neutron diffraction studies to answer the question of a high-temperature form of Pr_9O_{16}.

CONCLUSION

The structure of the low-temperature form of Pr_9O_{16} has been refined through powder neutron TOF diffraction and Rietveld analysis. The model proposed previously on the basis of electron microscopy and image simulation has been proved to be correct. This structure contains

double vacancy clusters, which are similar to those in Pr_7O_{12}. The double vacancy clusters may be considered a condensation dimer of single coordination defects. Furthermore, Pr_9O_{16} can be related to Pr_7O_{12} and Tb_7O_{12} since they share in common (010) slabs (i.e., the $(1\bar{5}\bar{3})_F$ planes) of double-vacancy defect clusters. These slabs are closely packed in the former and separated in the latter by a layer of "PrO_2." The existence of the high-temperature form of Pr_9O_{16} has not been confirmed and further studies involving *in situ*, high-temperature observations are required.

ACKNOWLEDGMENTS

It is a pleasure to acknowledge the patient tutorial help of D. J. M. Bevan in understanding the intricacies of these complex fluorite-related structures, extending even to his refereeing of this paper. We thank the National Science Foundation for financial support through Research Grant DMR-9114799 and the Manuel Lujan, Jr. Neutron Scattering Center, funded in part by the Office of Basic Energy Sciences Division of Materials Sciences of the U.S. Department of Energy (Contract W-7405-ENG-36).

REFERENCES

1. L. Eyring, *in* "Handbook on the Physics and Chemistry of Rare Earths" (K. A. Gschneidner, Jr. and L. Eyring, Eds.), Vol. 3, p. 337. North-Holland, Amsterdam, 1979.
2. D. J. M. Bevan, *J. Inorg. Nucl. Chem.* **1,** 49 (1955).
3. R. E. Ferguson, E. D. Guth, and L. Eyring, *J. Amer. Chem. Soc.* **76,** 3890 (1954).
4. E. D. Guth and L. Eyring, *J. Am. Chem. Soc.* **16,** 5245 (1954).
5. G. Brauer, *in* "Progress in the Science and Technology of the Rare Earths" (L. Eyring, Ed.), Vol. 2, p. 312. Pergamon Press, Oxford, 1966.
6. J. O. Sawyer, B. G. Hyde, and L. Eyring, *Bull. Soc. Chim. Fr.* No. 149, 152 (1965).
7. R. P. Turcotte, M. S. Jenkins, and L. Eyring, *J. Solid State Chem.* **7,** 454 (1973).
8. P. Kunzmann and L. Eyring, *J. Solid State Chem.* **14,** 229 (1975).
9. R. L. Martin, *J. Chem. Soc. Dalton Trans.*, 1335 (1974).
10. B. F. Hoskins and R. L. Martin, *J. Chem. Soc. Dalton Trans.*, 576 (1975).
11. B. F. Hoskins and R. L. Martin, *J. Chem. Soc. Dalton Trans.*, 676 (1976).
12. O. T. Sørensen, *NATO ASI Ser., C* **276,** 123 (1988).
13. E. Schweda, D. J. M. Bevan, and L. Eyring, *J. Solid State Chem.* **90,** 109 (1991).
14. R. B. Von Dreele, L. Eyring, A. L. Bowman, and J. L. Yarnell, *Acta Crystallogr. Sect. B* **31**(4), 971 (1975).
15. S. P. Ray, A. S. Nowick, and D. E. Cox, *J. Solid State Chem.* **15,** 344 (1975).
16. A. C. Larson, and R. B. Von Dreele, "GSAS—General Structure Analysis System," Los Alamos National Laboratory Report LA-UR 86-748, 1986.
17. J. Zhang, R. B. Von Dreele, and L. Eyring, *J. Solid State Chem.* **104,** 21 (1993).
18. R. T. Tuenge and L. Eyring, *J. Solid State Chem.* **29,** 165 (1979).
19. R. D. Shannon, *Acta Crystallogr. Sect. A* **32,** 751 (1976).
20. M. R. Thornber and D. J. M. Bevan, *J. Solid State Chem.* **1,** 536 (1970).
21. R. C. Karnatak, J. M. Esteva, H. Dexpert, M. Gasgnier, P. E. Caro, and L. Albert, *Phys. Rev. B* **36,** 1745 (1987).
22. L. Eyring and N. C. Baenziger, *J. Appl. Phys. Suppl.* **33,** 428 (1962).
23. B. Hyde and L. Eyring, *in* "Proceedings, 4th Conf. Rare Earth Research, Phoenix, AZ, 1964" (L. Eyring, Ed.), p. 623. Gordon and Breach, New York, 1965.
24. M. R. Thornber, D. J. M. Bevan, and J. Graham, *Acta Crystallogr. Sect. B* **24,** 1183 (1968).
25. H. J. Rossell, *Adv. Ceram.* **3,** 47 (1981).
26. J. Zhang, Z. C. Kang, and L. Eyring, *J. Alloys Compounds* **192,** 57 (1993).
27. J. Zhang, R. B. Von Dreele, and L. Eyring, unpublished research, 1992.